CrystEngComm

ROYAL SOCIETY OF CHEMISTRY

PAPER

View Article Online
View Journal | View Issue

Cite this: *CrystEngComm*, 2021, **23**, 7970

Temperature-dependent crystallization of Cu_2O rhombic dodecahedra†

Zhiqiang Wang,[a] Wangzhu Cao,[a] Kunfeng Chen *[a] and Dongfeng Xue *[b]

Received 24th February 2021,
Accepted 15th April 2021

DOI: 10.1039/d1ce00273b

rsc.li/crystengcomm

Size and shape uniformity of nanomaterials are extremely important for their applications in batteries, supercapacitors, catalysis, *etc.* In the crystallization process, finding proper synthesis conditions is necessary to have control over size dispersion, as well as crystal planes. In this work, we synthesized Cu_2O rhombic dodecahedra (exposing 12 {110} planes) with size range from 1351 nm to 142 nm at a reaction temperature of 31–60 °C. The main parameters governing the size of Cu_2O were the concentration of the precursor species and reduction reaction, which were affected by a given temperature. Results of crystallization experiments indicated that reaction and crystallization kinetics were mainly enhanced by raised temperature. Serving as lithium ion battery anodes, Cu_2O rhombic dodecahedra showed higher capacity than cubes and octahedra. This work gives us a way of optimizing the temperature conditions for obtaining size uniformity of nanomaterials.

1. Introduction

In modern materials science and engineering, the morphology, particle size, orientation and nanostructure of metal oxides have significant effects on their catalytic, magnetic and electronic properties.[1–5] Therefore, it is critical to effectively control the size and morphology of metal oxides during the crystallization process. Many works have been devoted to controlling the size of particles from nanometer to micrometer, and various morphologies have been successfully synthesized, such as wires,[6] rods,[7] cubes[8] and octahedra.[9] To control the size and morphology of the particles, it is important and meaningful to study the nucleation and growth mechanisms of nanocrystals, which are the most important processes of crystallization. According to crystallization theory, the variables that affect the growth rate are supersaturation, temperature and interfacial tension.[10] Temperature has a significant impact on controlling the nucleation and growth process, which can affect the size and shape of materials. Studying the relationship between the morphology/size of nanoparticles and reaction temperature is of great significance for the realization of tunable design and preparation of functional materials.

Due to its advantages of facile synthesis and the available customized morphologies, Cu_2O has been widely studied in the fields of electrocatalysis,[11] gas sensors,[12] antibacterial agents,[13] and electrochemical energy storage.[14] The crystallization of Cu_2O nanostructures with precise size and shape control can provide a potential opportunity to discover unique morphology-related properties. The typical polyhedral shapes of Cu_2O are cubes (c-Cu_2O, six {100} planes), octahedra (o-Cu_2O, eight {111} planes), rhombic dodecahedra (d-Cu_2O, twelve {110} planes), and other polyhedra with different ratios of exposed {100}, {111}, {110} crystal planes. Recently, many researchers have directed a lot of effort at gaining insight into the relationship between the crystal planes and properties of Cu_2O. For example, Chen *et al.*[15] have studied the sensor sensitivity of c-Cu_2O and o-Cu_2O for different kinds of organic gases, and the results displayed that o-Cu_2O had enhanced sensing performance. Wang *et al.*[16] showed that o-Cu_2O exhibited higher activity in killing *E. coli* than c-Cu_2O due to the different Cu/O atom arrangements of {111} and {100} facets.

Lithium-ion batteries are widely used electrochemical devices due to their high energy, power density and long cycle lifetime.[17–20] In order to obtain higher energy density and longer cycling life, the chemical activity and reversibility of anode materials have been studied in detail, for example, Fe_2O_3,[21] TiO_2,[22] Co_3O_4,[23] NiO (ref. 24), Cu_2O,[25] *etc.* Owing to its controllable size and morphology, Cu_2O is often used to study the size- and morphology-dependent electrochemical energy storage properties. The high-energy crystal plane has more surface dangling atoms, which will promote the reaction between Cu_2O and lithium, so Cu_2O polyhedra with

[a] *State Key Laboratory of Crystal Materials, Institute of Crystal Materials, Shandong University, Jinan 250100, China. E-mail: Kunfeng.Chen@sdu.edu.cn*
[b] *Multiscale Crystal Materials Research Center, Shenzhen Institute of Advanced Technology, Chinese Academy of Sciences, Shenzhen 518055, China. E-mail: df.xue@siat.ac.cn*

† Electronic supplementary information (ESI) available. See DOI: 10.1039/d1ce00273b

high-energy surface should have useful electrochemical properties. The surface energy of the three low-index crystal planes {100}, {111} and {110} of Cu_2O is closely related to the density of undercoordinated Cu atoms.[26] The {110} facet of d-Cu_2O has the maximum surface energy, which may result in d-Cu_2O having higher electrochemical capacity than c-Cu_2O and o-Cu_2O. In this work, Cu_2O with different size and shape was firstly crystallized by controlling the reaction temperature. Then, the relationship between the size/shape of d-Cu_2O and electrochemical properties was also studied. This work can provide some understanding about how specific reaction conditions lead to particular materials.

2. Experimental section

Synthesis of Cu_2O cubes

50 mmol PEG-200, 2 mmol $CuSO_4{\cdot}5H_2O$, 2.5 mmol sodium ascorbate and 75 mmol NaOH were dissolved in 800 mL, 200 mL, 500 mL and 500 mL water, respectively. Then, the copper(II) solution was added to the PEG-200 solution. The mixed solution of sodium ascorbate and NaOH was added into the copper(II) solution. After vigorous stirring for 20 min, the yellow precipitates were filtered off and dried at 35 °C for further characterization.

Synthesis of Cu_2O rhombic dodecahedra

69.2 mL deionized water was added into a sample bottle, and placed in a water bath at a given temperature. After heating for a while, 0.5 mL of 0.1 M $CuCl_2$ solution was added into the deionized water, and then 0.81 g SDS powder was added with vigorous stirring. 1.8 mL of 1.0 M NaOH was added to the above solution after complete dissolution of SDS. Then hydroxylamine hydrochloride solution was added into the sample bottle. After vigorous stirring for 60 min in the water bath, the precipitates were filtered off and dried at 35 °C for further characterization.

Synthesis of Cu_2O octahedra

0.4 g $CuSO_4{\cdot}5H_2O$ and 0.8 g PVP were dissolved in 70 mL water with vigorous stirring. 0.3 g NaOH was dissolved in 10 mL water and 0.4 mL of 50% N_2H_4 was added into the NaOH solution. Then, the above two solutions were mixed with vigorous stirring for 30 min. Precipitates were obtained and centrifuged between 2000 and 3000 rpm.

Characterization

The as-obtained products were investigated by scanning electron microscopy (SEM, JEOL, JSM-6700F), X-ray diffraction (XRD, Rigaku, Smartlab 3KW), X-ray photoelectron spectroscopy (XPS, Thermo ESCALAB250i) and Fourier transform infrared (FTIR) spectroscopy (IRAffinity-1S).

The lithium ion battery properties of Cu_2O were characterized by employing CR2032 coin cells. Working electrodes were fabricated by mixing Cu_2O products, polyvinylidene fluoride and carbon black in a weight ratio of 80 : 10 : 10. Then the mixed powders were adhered together by using *N*-methyl-2-pyrolidone, and coated onto copper foils. A lithium metal sheet was used as the counter electrode and a glass microfiber as separator. The electrolyte was 1 M $LiPF_6$ dissolved in a dimethyl carbonate and ethylene carbonate (DMC : EC = 1 : 1) solvent mixture. Electrochemical impedance spectroscopy (EIS) and cyclic voltammogram (CV) measurements were conducted with an electrochemical workstation (CHI 660E) over the potential range 0.01–3.0 V (*vs.* Li^+/Li), and charge–discharge tests of the Cu_2O/Li coin cells were carried out with a CT3001A battery test system (LANHE) at a set of current densities within the potential range 0.01–3.0 V (*vs.* Li^+/Li).

3. Results and discussion

Growth of d-Cu_2O

In order to investigate the growth process of d-Cu_2O, a series of samples produced with different reaction times were studied. Fig. 1a shows a schematic diagram of the size and morphology of d-Cu_2O for different reaction times at given temperature. In a typical process, after adding NaOH solution to the mixed solution of $CuCl_2$ and SDS, the solution quickly turned blue indicating the formation of $Cu(OH)_2$ and $[Cu(OH)_4]^{2-}$. The chemical reactions of this process are as follows:

$$Cu^{2+} + 2OH^- \rightarrow Cu(OH)_2 \quad (1)$$

$$Cu^{2+} + 4OH^- \rightarrow [Cu(OH)_4]^{2-} \quad (2)$$

After addition of $NH_2OH{\cdot}HCl$ into the mixture, the solution turned green and it lasted 30 s. The reaction can be shown as follows:

$$2NH_2OH + 2Cu(OH)_2 \rightarrow Cu_2O + N_2 + 5H_2O \quad (3)$$

The color changes of the solution in the synthesis process of d-Cu_2O are shown in Fig. S1.† The SEM image of the product obtained for a 30 s reaction time is shown in Fig. 2a; the small particles are Cu_2O nanoparticles and the floccule is $Cu(OH)_2$. This can be confirmed by the FTIR spectra in Fig. 3. Six characteristic peaks were located at 3572, 2916, 2849, 1612, 1263 and 624 cm^{-1}. The 3572 and 624 cm^{-1} peaks correspond to $Cu(OH)_2$ (ref. 27) and Cu_2O,[28] respectively. The peaks located at 2916, 2849 and 1247 cm^{-1} correspond to SDS.[29] The 1612 cm^{-1} peak is the H–O bending vibration of inevitably adsorbed water.[30] The green color change of the solution was because of the yellow of small Cu_2O particles,[31] and the blue of flocculent $Cu(OH)_2$. With an extension of the reaction time, $Cu(OH)_2$ was gradually consumed. When the reaction time reached 1 min, the yellow color of Cu_2O particles dominated in the solution owing to the disappearance of $Cu(OH)_2$ (Fig. 2b and 3). As the reaction time continued to increase, the particles continued to grow and formed integral d-Cu_2O, and the color of the solution

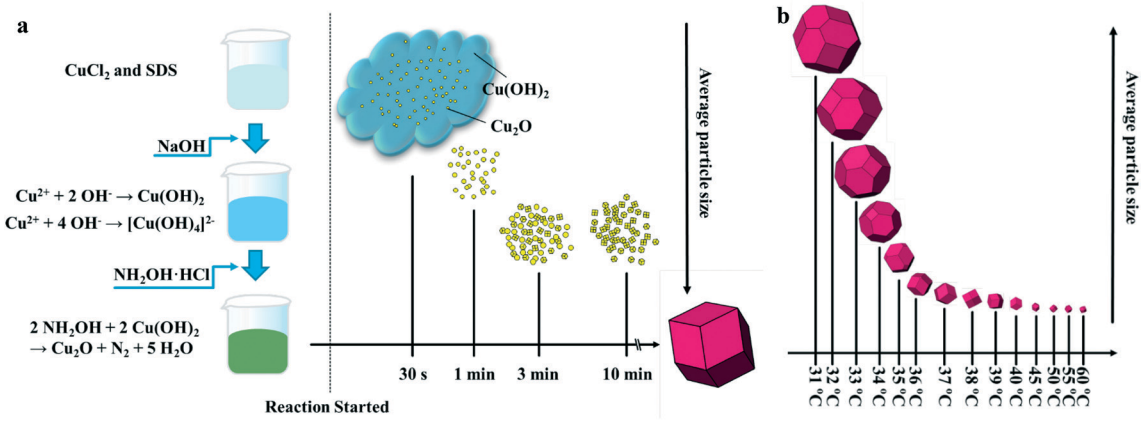

Fig. 1 (a) Schematic diagram of particle size and morphology evolution of d-Cu_2O with increasing reaction time synthesized at a specific temperature. (b) Schematic diagram of particle size and morphology evolution of d-Cu_2O with increasing synthesis temperature.

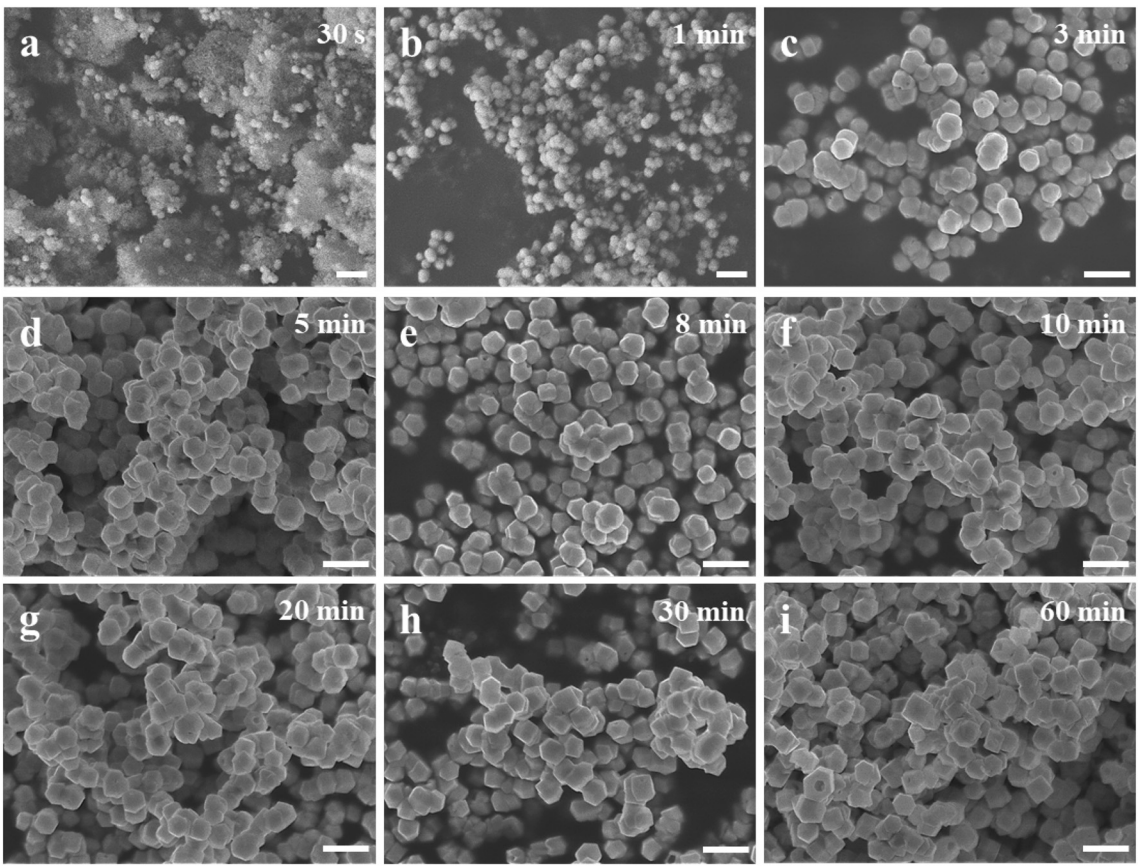

Fig. 2 SEM images of d-Cu_2O nanoparticles synthesized using a 40 °C water bath with different reaction times: (a) 30 s, (b) 1 min, (c) 3 min, (d) 5 min, (e) 8 min, (f) 10 min, (g) 20 min, (h) 30 min and (i) 60 min. Scale bars = 500 nm.

also changed to orange (Fig. 2 and S1†). After the reaction time reached 60 min, a single peak at 611 cm^{-1} in the FTIR spectrum was present, which is close to the Cu_2O single-crystal peak at 610 cm^{-1}.[32] The other peaks located at 3444, 3336 and 1612 cm^{-1} were attributed to the H–O bending vibration from adsorbed water.[30,33,34] The relationship between the size of d-Cu_2O and the reaction time is shown in Table S2† and Fig. 4a.

Fig. 1b shows a schematic diagram of the temperature dependence of morphology and size of d-Cu_2O. As shown in Fig. 5, the morphology and size of d-Cu_2O change with reaction temperature. As the reaction temperature increases, the exposed {100} crystal plane gradually became smaller, and finally a complete rhombic dodecahedron was formed at 37 °C (Fig. 5g), which may be due to the accelerated growth of {100} crystal planes when the temperature was increased.[35]

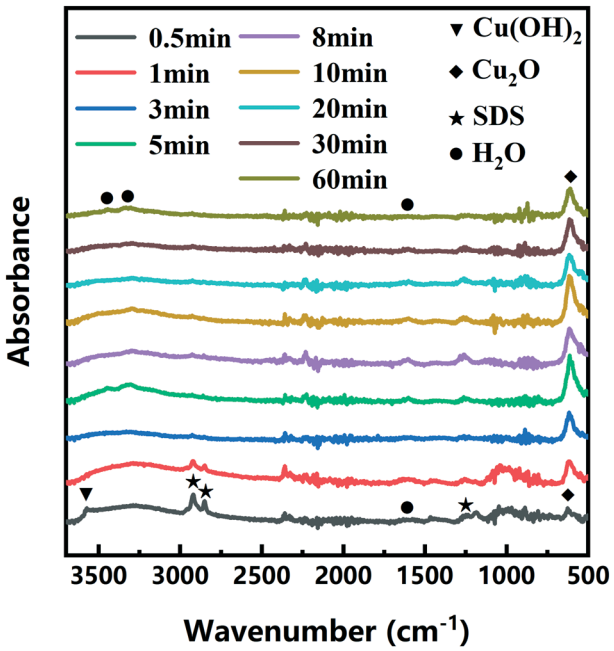

Fig. 3 FTIR spectra of d-Cu_2O obtained at different reaction times using a 40 °C water bath.

At the same time, the average particle sizes of the products gradually decreased as the temperature increased, indicating that the nucleation process was affected by the reaction temperature. According to classical nucleation theory, nucleation is enhanced as temperature increases.[4] As the temperature increases, the critical nucleus radius decreases, while the number of nuclei increases, which may lead to a smaller grain size. The corresponding average particle size at each temperature is shown in Table S3.† Fig. 4b clearly illustrates the relationship between particle size and temperature. The colors of products obtained at different temperatures are also different. d-Cu_2O changes from brick red to yellow as the reaction temperature increases, as shown in Fig. S2,† which is mainly caused by the change of particle size.

Purity analysis and electrochemical performance test

c-Cu_2O (~150 nm) and o-Cu_2O (50–160 nm) were successfully synthesized by different reaction systems (Fig. S3†). Fig. 6 shows the XRD patterns of three as-prepared products and that of the standard card of Cu_2O (JCPDS No. 05-667). The XRD patterns of d-Cu_2O synthesized at different temperatures are shown in Fig. S4.† The diffraction peaks at 29.57, 36.42, 42.31, 52.46, 61.38, 73.52 and 77.37° correspond to (110), (111), (200), (211), (220), (311) and (222) planes of Cu_2O, verifying the successful synthesis of pure phase Cu_2O with three morphologies. All diffraction peaks are sharp, indicating that the prepared products have high crystallinity.

The electrochemical performances of d-Cu_2O, c-Cu_2O and o-Cu_2O were evaluated as anode materials for lithium-ion batteries. The discharge and charge curves measured at a current density of 100 mA g^{-1} are shown in Fig. S5.† The first discharge capacities of d-Cu_2O (synthesized at 31–40 °C), c-Cu_2O and o-Cu_2O are 641.2, 715.5, 788.4, 813.5, 578.6, 642.4, 737.1, 642.8, 612.5, 795.3, 545.8 and 657.4 mA h g^{-1}, respectively. Fig. 7a shows the rate and cycling performances of all samples. The d-Cu_2O samples synthesized at different temperatures exhibit different rate performances. With an increase of temperature, the capacity increases, while as the temperature rises above 37 °C, the capacity decreases. It can be clearly seen that d-Cu_2O synthesized at 35 °C showed the best rate cycling performance. Small-sized d-Cu_2O often displays higher capacity owing to larger surface area that can provide more active sites for Li reaction. It is worth noting that the morphology of the sample synthesized at 35 °C was not complete rhombic dodecahedra, but polyhedra with a small area of exposed {100} plane. Fig. 5g shows the complete

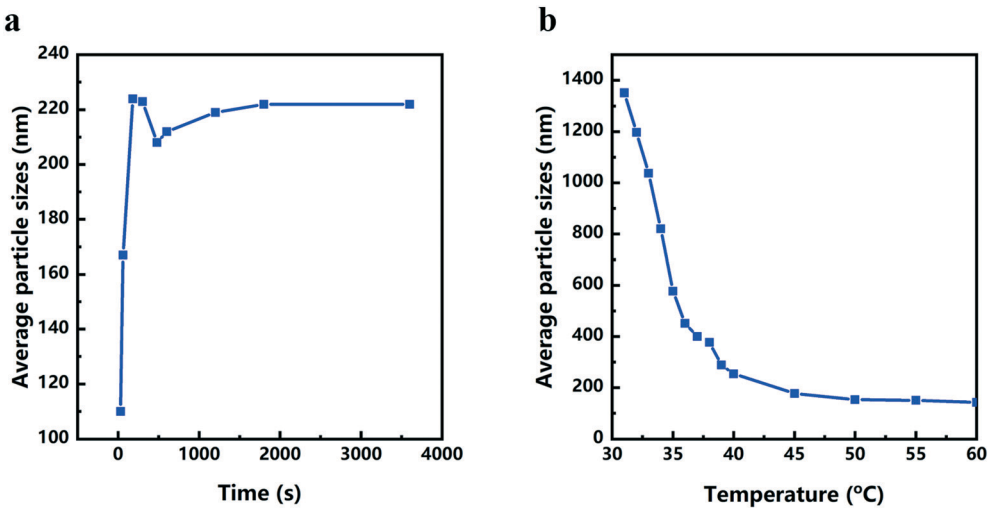

Fig. 4 (a) Reaction time dependence of average particle size of d-Cu_2O obtained at a synthesis temperature of 40 °C. (b) Reaction temperature dependence of the average particle size of d-Cu_2O after reaction of 1 h.

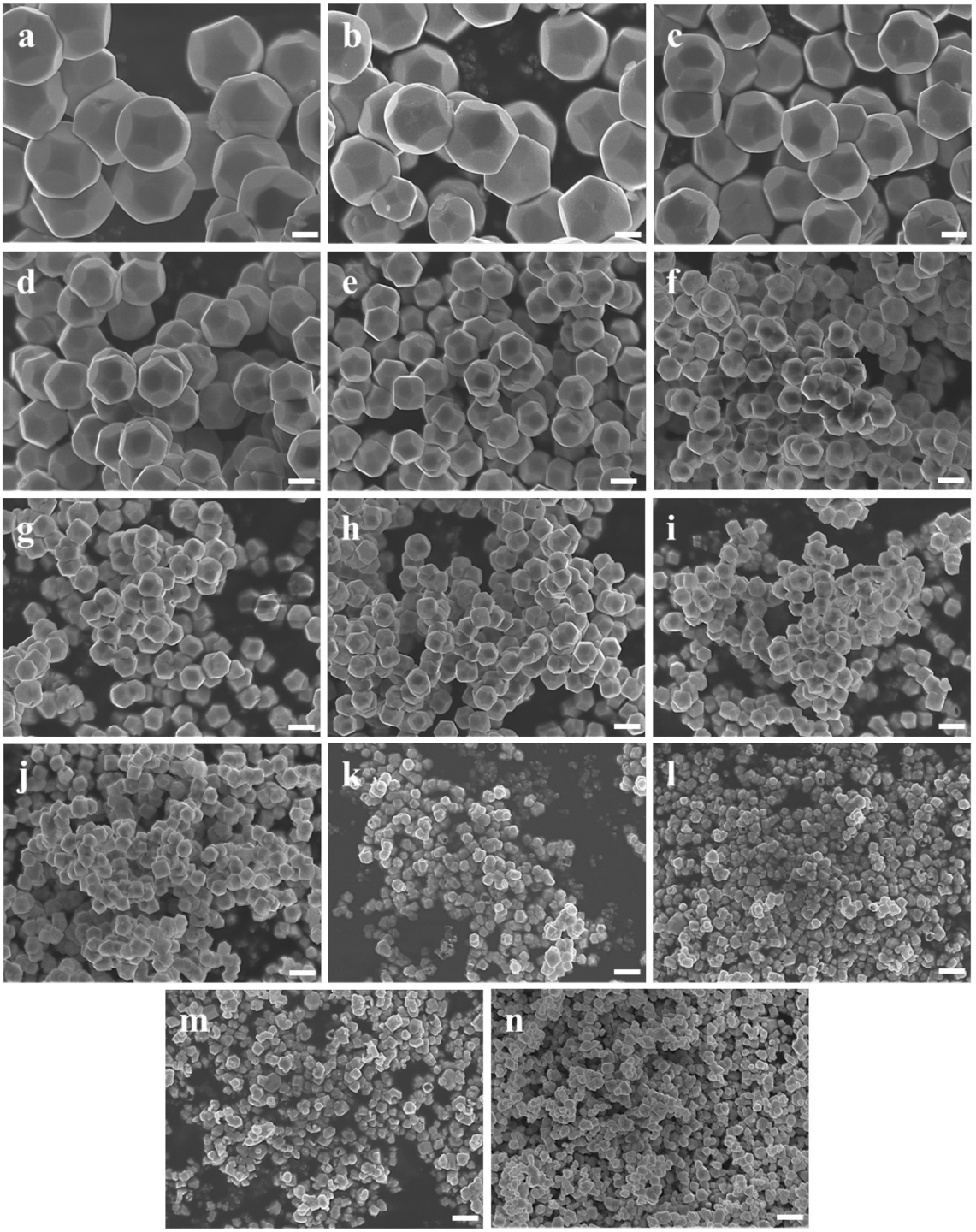

Fig. 5 SEM images of d-Cu_2O synthesized at different temperatures: (a) 31 °C, (b) 32 °C, (c) 33 °C, (d) 34 °C, (e) 35 °C, (f) 36 °C, (g) 37 °C, (h) 38 °C, (i) 39 °C, (j) 40 °C, (k) 45 °C, (l) 50 °C, (m) 55 °C and (n) 60 °C. Scale bars = 500 nm.

rhombohedral dodecahedra formed at 37 °C. The discharge capacities of d-Cu_2O (synthesized at 37 °C), c-Cu_2O and o-Cu_2O are shown in Fig. 7b. It can be concluded that d-Cu_2O with exposed {110} crystal plane has the largest discharge capacity, which is greater than that of c-Cu_2O with exposed {100} crystal plane, and that of o-Cu_2O with exposed {111} crystal plane. Owing to c-Cu_2O and o-Cu_2O having small sizes (Fig. S3†), the particle size effect on lithium ion battery performances between c-Cu_2O, o-Cu_2O and d-Cu_2O is not prominent. But, the crystal plane effect is important for their electrochemical performances.

After the cycling tests at a current density of 100 mA g^{-1}, the discharge capacities of d-Cu_2O, c-Cu_2O and o-Cu_2O are 400.8, 415.2 and 350.3 mA h g^{-1}, respectively. It is very

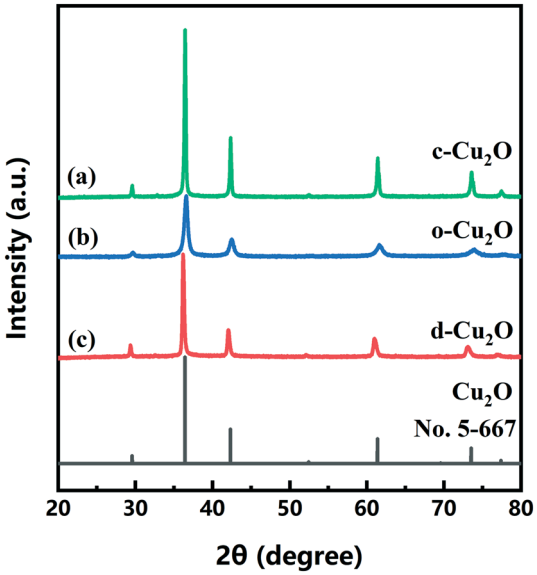

Fig. 6 XRD patterns of (a) c-Cu_2O, (b) o-Cu_2O and (c) d-Cu_2O (synthesized at 40 °C). The XRD pattern of standard card of Cu_2O (JCPDS 5-667) is also shown.

interesting that the discharge capacities of d-Cu_2O and c-Cu_2O samples are higher than the theoretical capacity. In fact, this phenomenon occurs mainly because of phase transition from Cu_2O to CuO (ref. 14) (the theoretical capacity of CuO is 674 mA h g^{-1}), which can be confirmed from Cu $2p_{3/2}$ XPS spectra (Fig. S6†). The peaks detected at 932.2 and 933.6 eV for the cycled electrode material are related to Cu/Cu_2O and CuO, respectively.[36,37]

Studying the charge and discharge mechanism of Cu_2O electrode materials is of great significance. The CV curves of d-Cu_2O (reaction temperatures from 31 to 40 °C), c-Cu_2O and o-Cu_2O were obtained at a scan rate of 0.2 mV s^{-1} within the potential range of 0.01 to 3.0 V (*vs.* Li^+/Li), as shown in Fig. S7.† In the cathodic polarization of the 1st cycle, all the samples exhibit two obvious reduction peaks at 1.5–1.0 V and 1.0–0.5 V, respectively, at a scan rate of 0.2 mV s^{-1}. In the oxidation polarization process of the 1st cycle, all the samples exhibit two oxidation peaks at 0.7–1.7 V and 2.3–2.7 V. According to previous research, the electrochemical redox reactions of Cu_2O are as follows:[36]

$$Cu_2O + 2Li^+ + 2e^- \rightarrow Li_2O + 2Cu \quad (4)$$

$$2Li_2O + 3Cu \rightarrow Cu_2O + 4Li + CuO \quad (5)$$

Two pairs of redox peaks corresponded to eqn (4) and (5), respectively. The peaks below 0.2 V can be ascribed to the formation and decomposition of solid electrolyte interface.[37,38] In the cathodic polarization process of the 2nd cycle, there are two reduction peaks in the range of 1.0–2.7 V. The corresponding equations for the peaks of high voltage and low voltage are eqn (6) and (7), respectively:

$$2CuO + 2Li^+ + 2e^- \rightarrow Cu_2O + Li_2O \quad (6)$$

$$Cu_2O + 2Li^+ + 2e^- \rightarrow Li_2O + 2Cu \quad (7)$$

As shown in Fig. 8a–c, CV tests of d-Cu_2O, c-Cu_2O and o-Cu_2O were carried out at different scanning rates after activation at 0.2 mV s^{-1} for three cycles. The relationships between ln(current) and ln(scan rate) of d-Cu_2O, c-Cu_2O and o-Cu_2O are shown in Fig. 8d. The slopes were calculated using eqn (8):

$$I = a\nu^b \quad (8)$$

where I and ν are current and scan rate, respectively. The slopes of d-Cu_2O, c-Cu_2O and o-Cu_2O are 0.72, 0.94 and 0.82, respectively. The results demonstrate the capacities of d-

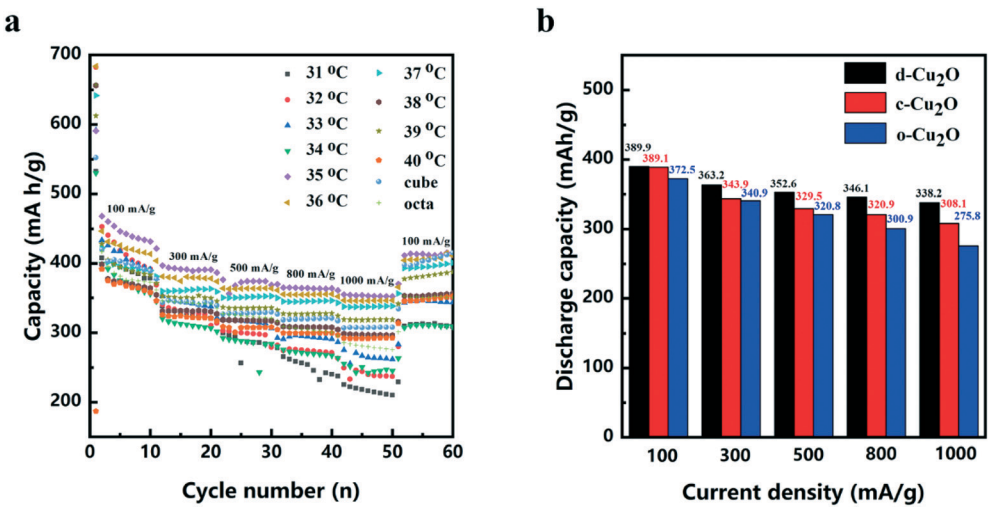

Fig. 7 (a) High rate cycling performance of d-Cu_2O (reaction temperatures from 31 to 40 °C), c-Cu_2O and o-Cu_2O. (b) Discharge capacity of d-Cu_2O (synthesized at 37 °C), c-Cu_2O and o-Cu_2O with the current density ranging from 100 to 1000 mA g^{-1}.

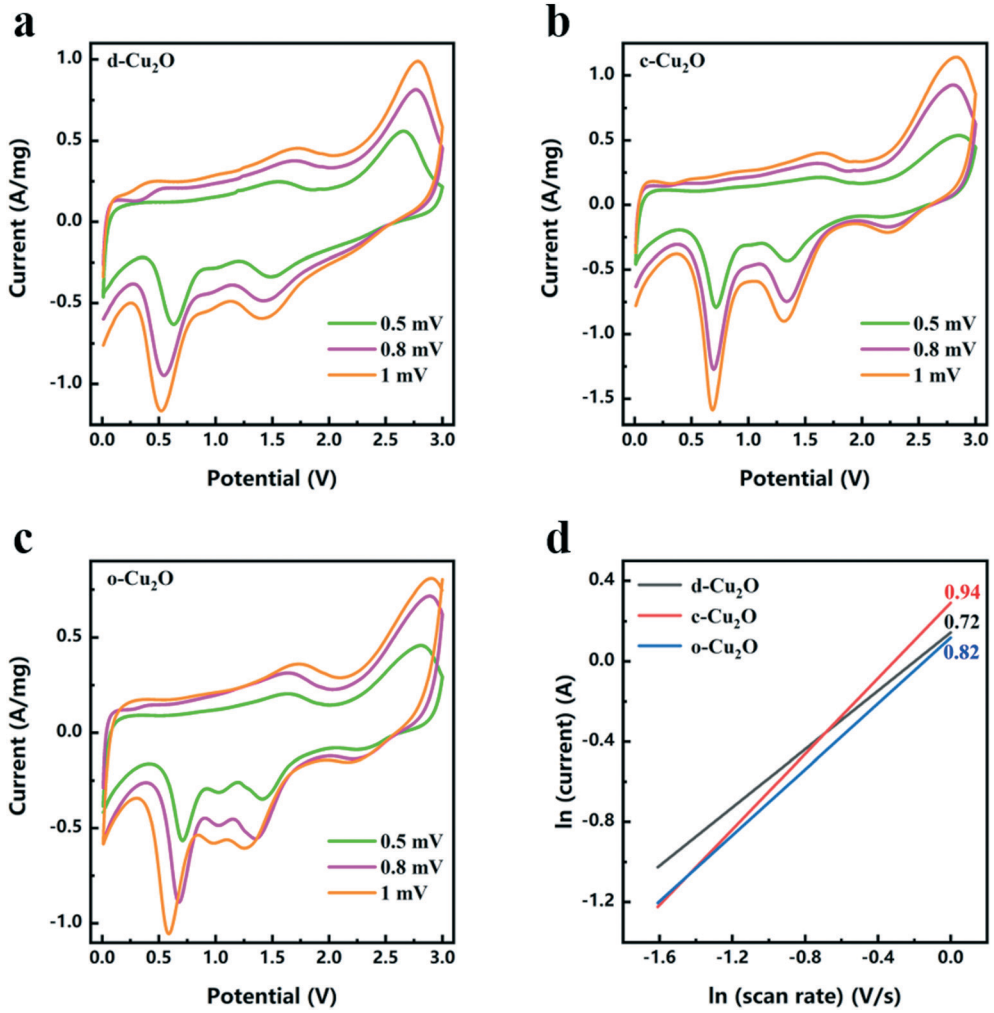

Fig. 8 CV curves of (a) d-Cu_2O, (b) c-Cu_2O, and (c) o-Cu_2O measured at different scanning rates from 0.5 to 1 mV s^{-1} after activation at 0.2 mV s^{-1} for three cycles. (d) Relationships between ln(current) and ln(scan rate) for d-Cu_2O, c-Cu_2O and o-Cu_2O (peaks of potential at 2.5–3 V).

Cu_2O, c-Cu_2O and o-Cu_2O are from both capacitive and battery contributions. Those of o-Cu_2O and c-Cu_2O are mainly from capacitive contribution, while for d-Cu_2O there is a small contribution of capacitive capacity.

The Nyquist plots of d-Cu_2O, c-Cu_2O and o-Cu_2O were measured in the frequency range of 10^{-2}–10^5 Hz. In general, R_Ω and R_{ct} correspond to the electrolyte resistance and interface charge transfer resistance, respectively.[39] From Fig. S8,† the values of R_Ω/R_{ct} of d-Cu_2O c-Cu_2O and o-Cu_2O are 4.29/36.79, 4.89/44.35 and 5.23/51.44 Ω, respectively. The values of R_Ω/R_{ct} of d-Cu_2O are obviously less than those of c-Cu_2O and o-Cu_2O. According to the rate and EIS results, d-Cu_2O displayed better kinetic performance.

4. Conclusions

In conclusion, this work showed that the sizes and morphologies of d-Cu_2O were a function of temperature. Cu^{2+} reduction reaction, phase transformation ($Cu(OH)_2$ → Cu_2O) and nucleation-growth (d-Cu_2O, c-Cu_2O and o-Cu_2O) occurred during the Cu_2O crystallization. Increasing temperature mainly affected the reduction reaction and nucleation processes. Thus, more nuclei were formed at high temperature leading to the Cu_2O size decreasing from 1351 nm to 142 nm with solution temperature increasing from 31 to 60 °C. In most crystallization experiments, the size increased to maximum value within a reaction time of about 200 s. It is important to subtly control the solution temperature and reaction time for size control and size uniformity. Serving as a lithium ion battery anode, d-Cu_2O with exposed {110} crystal plane has the largest discharge capacity, which is greater than that of c-Cu_2O with exposed {100} crystal plane and o-Cu_2O with exposed {111} crystal plane. This work gives us an inspiration for optimizing the temperature of the facile synthesis to obtain size uniformity for large-scale industrial applications.

Conflicts of interest

There are no conflicts to declare.

Acknowledgements

This work was supported by National Natural Science Foundation of China (51832007) and Natural Science Foundation of Shandong Province (ZR2020ZD35). K. C. also acknowledges Qilu Young Scholars Program of Shandong University.

References

1 C. Arcangeli, P. Circelli, M. Donini, A. A. Aljabali, E. Benvenuto, G. P. Lomonossoff and C. Marusic, *J. Biomol. Struct. Dyn.*, 2014, **32**, 630–647.
2 J. Hu, M. Chen, X. Fang and L. Wu, *Chem. Soc. Rev.*, 2011, **40**, 5472–5491.
3 P. Liu, Y. Huang and X. Zhang, *J. Alloys Compd.*, 2014, **596**, 25–31.
4 X. Wang, M. Chen, Y. He and J. Zhu, *J. Alloys Compd.*, 2015, **628**, 50–56.
5 B. R. Cuenya, *Thin Solid Films*, 2010, **518**, 3127–3150.
6 M. Zhang, M. Drechsler and A. H. E. Müller, *Chem. Mater.*, 2004, **16**, 537–543.
7 X. Liu, Z. Jin, S. Bu, J. Zhao and K. Yu, *Mater. Sci. Eng., B*, 2006, **129**, 139–143.
8 Y. Sun, *Science*, 2002, **298**, 2176–2179.
9 W. Yu, T. Zhang, J. Zhang, X. Qiao, L. Yang and Y. Liu, *Mater. Lett.*, 2006, **60**, 2998–3001.
10 R. A. Judge, R. S. Jacobs, T. Frazier, E. H. Snell and M. L. Pusey, *Biophys. J.*, 1999, **77**, 1585–1593.
11 X. W. Liu, *Langmuir*, 2011, **27**, 9100–9104.
12 Z. Xie, N. Han, W. Li, Y. Deng, S. Gong, Y. Wang, X. Wu, Y. Li and Y. Chen, *Phys. Status Solidi A*, 2017, **214**, 1600904.
13 X. T. Shi, C. W. Xue, F. Fang, X. W. Song, F. Yu, M. X. Liu, Z. P. Wei, X. Fang, D. X. Zhao, H. B. Xin and X. L. Wang, *ACS Appl. Mater. Interfaces*, 2016, **8**, 8386–8392.
14 K. Chen, S. Song and D. Xue, *CrystEngComm*, 2015, **17**, 2110–2117.
15 M. Chen, Y. Wang, Y. Zhang, Y. Yuan, J. Liu, B. Liu, Q. Du, Y. Ren and H. Yang, *Sens. Actuators, B*, 2020, **310**, 127827.
16 J. Ren, W. Wang, S. Sun, L. Zhang, L. Wang and J. Chang, *Ind. Eng. Chem. Res.*, 2011, **50**, 10366–10369.
17 A. Manthiram, *Nat. Commun.*, 2020, **11**, 1550.
18 Z. Deng, X. Lin, Z. Huang, J. Meng, Y. Zhong, G. Ma, Y. Zhou, Y. Shen, H. Ding and Y. Huang, *Adv. Energy Mater.*, 2021, **11**, 2000806.
19 W. Yu, Z. Hu, M. Yi, S. Huang, D. Chen, J. Jin, Y. Li, G. Van Tendeloo and B. Su, *RSC Adv.*, 2016, **6**, 97129–97136.
20 L. Zhang, Q. Li, H. Xue and H. Pang, *ChemSusChem*, 2018, **11**, 1581–1599.
21 C. Ding, Y. Zeng, R. Li, Y. Zhang and L. Zhao, *J. Alloys Compd.*, 2016, **676**, 347–355.
22 G. Wang, Y. Sui, M. Zhang, M. Xu, Q. Zeng, C. Liu, X. Liu, F. Du and B. Zou, *J. Mater. Chem. A*, 2017, **5**, 18577–18584.
23 G. L. Xu, J. T. Li, L. Huang, W. F. Lin and S. G. Sun, *Nano Energy*, 2013, **2**, 394–402.
24 D. Xie, Q. Su, W. Yuan, Z. Dong, J. Zhang and G. Du, *J. Phys. Chem. C*, 2013, **117**, 24121–24128.
25 K. Chen, S. Song and D. Xue, *CrystEngComm*, 2013, **15**, 144–151.
26 Y. Shang and L. Guo, *Adv. Sci.*, 2015, **2**, 1500140.
27 K. Okada, R. Ricco, Y. Tokudome, M. J. Styles, A. J. Hill, M. Takahashi and P. Falcaro, *Adv. Funct. Mater.*, 2014, **24**, 1969–1977.
28 M. Balık, V. Bulut and I. Y. Erdogan, *Int. J. Hydrogen Energy*, 2019, **44**, 18744–18755.
29 T. Bala, R. D. Gunning, M. Venkatesan, J. F. Godsell, S. Roy and K. M. Ryan, *Nanotechnology*, 2009, **20**, 415603.
30 Z. Gao, J. Liu, F. Xu, D. Wu, Z. Wu and K. Jiang, *Solid State Sci.*, 2012, **14**, 276–280.
31 L. Huang, F. Peng, H. Yu and H. Wang, *Solid State Sci.*, 2009, **11**, 129–138.
32 A. Jagminas, G. Niaura, J. Kuzmarskyt and R. Butkien, *Appl. Surf. Sci.*, 2004, **225**, 302–308.
33 L. Zhang, P. Ying, B. Yu, L. Wu, J. Wang, X. Gu, S. Chen, R. Zhou and Z. Ni, *RSC Adv.*, 2014, **4**, 42892–42898.
34 A. S. Katkar and P. V. Shelar, *Int. J. Chem. Phys. Sci.*, 2018, **7**, 75–80.
35 X. Yang, S. Zhang, L. Zhang, B. Zhang and T. Ren, *RSC Adv.*, 2019, **9**, 36831–36837.
36 M. Kim, S. Kim, S. Han, D. Kwak, E. Hwang, D. Kim, G. Lee, H. Choe and K. Park, *J. Mater. Chem. A*, 2015, **3**, 23003–23010.
37 Y. H. Lee, I. C. Leu, C. L. Liao, S. T. Chang, M. T. Wu, J. H. Yen and K. Z. Fung, *Electrochem. Solid-State Lett.*, 2006, **9**, A207.
38 Y. Xu, Y. Guo, C. Li, X. Zhou, M. C. Tucker, X. Fu, R. Sun and C. Wong, *Nano Energy*, 2015, **11**, 38–47.
39 W. Cao, K. Chen and D. Xue, *Materials*, 2021, **14**, 510.